Journal of Alloys and Compounds 790 (2019) 716–722

Contents lists available at ScienceDirect

Journal of Alloys and Compounds

journal homepage: http://www.elsevier.com/locate/jalcom

Magnetic enhancement of carbon-encapsulated magnetite nanoparticles

Jiann-Shing Lee**, Yuan-Jhe Song, Hua-Shu Hsu, Chun-Rong Lin, Jing-Ya Huang, Jiunn Chen*

Department of Applied Physics, National Pingtung University, Pingtung 90003, Taiwan

ARTICLE INFO

Article history:
Received 24 December 2018
Received in revised form
29 January 2019
Accepted 12 March 2019
Available online 14 March 2019

Keywords:
Carbon encapsulation
Magnetite
Core-shell
Magnetic enhancement
Ferrimagnetic
Electronic structure
Charge transfer
Heterostructure
Band alignment

ABSTRACT

In this paper, we report the effect of carbon encapsulation on the magnetic behavior of magnetite (Fe_3O_4) nanoparticles obtained through chemical coprecipitation. Using starch, Fe_3O_4/carbon core–shell nanoparticles were produced through a hydrothermal method. Magnetic studies revealed that both the Fe_3O_4 and Fe_3O_4/carbon core–shell nanoparticles were nearly superparamagnetic at room temperature; more importantly, carbon encapsulation significantly enhanced the room-temperature ferrimagnetism. Transmitting optical magnetic circular dichroism analysis indicated the existence of interfacial charge transfer in the Fe_3O_4/carbon heterosystem. The ferrimagnetic enhancement was attributed to the charge transfer to polarized states of the *A*-site in Fe_3O_4, which is equivalent to chemical reduction of the *A*-site irons of Fe_3O_4. We concluded that Fe_3O_4/carbon core–shell nanoparticles formed a heterosystem so that the amorphous carbon passivated the magnetic semiconducting Fe_3O_4 nanoparticles, to which the sp^2 electron was transferred.

1. Introduction

Nanocomposite materials with extended functionality have drawn research attention due to their potential applications in chemistry and nanotechnology. Carbon encapsulation is a promising method for forming core–shell nanostructures because carbon is light weight, biocompatible, and thermally and chemically stable. Carbon-encapsulated magnetic nanoparticles (NPs) are interesting because of their potential biomedical applications [1–3]. Carbon encapsulation can mitigate chemical corrosion–induced instability and can modify the magnetic properties of core materials.

Magnetite (Fe_3O_4) has been extensively studied as a core material because of its ease of preparation and functionalization in the laboratory. Its superparamagnetism and low toxicity may enable Fe_3O_4 NPs to meet the growing demand for biomedical applications, such as diagnostic magnetic resonance imaging, thermal therapy, and drug delivery [4–8]. Fe_3O_4 NPs benefit biomedical applications because they are superparamagnetic [i.e., high saturation magnetization (M_s) and nearly zero coercivity] [9,10] at room temperature and are usually smaller than 20 nm. Nevertheless, Fe_3O_4 NPs often exhibit the chemical corrosion–induced instability, which may cause partial oxidation into γ-Fe_2O_3 [9,11]. To alleviate this, they can be coated with protective layers of various materials [12]. Such nanocomposite materials are primarily composed of Fe_3O_4 cores coated with organic or inorganic shells.

Fe_3O_4 is a soft ferrimagnetic material with low magnetic anisotropy at room temperature. Among iron oxides, it possesses the highest M_s (92 emu/g) at room temperature [13]. Magnetite crystallizes into a structure with a space group of $Fd\bar{3}m$ at room temperature. All iron cations are in the trivalent state in maghemite (γ-Fe_2O_3), whereas magnetite contains both Fe^{2+} and Fe^{3+} cations. The cell content of ideal magnetite is $[Fe^{3+}{}_8]_A[Fe^{3+}{}_8\ Fe^{2+}{}_8]_BO_{32}$, in which one-third of Fe ions are tetragonally coordinated with four oxygen atoms, and two-third of Fe ions are octahedrally coordinated with six oxygen atoms; which are called the *A*- and *B*-site, respectively. Magnetic moments of Fe ions in each site are

* Corresponding author.
** Corresponding author.
E-mail addresses: jslee@mail.nptu.edu.tw (J.-S. Lee), asesrrc@gmail.com (J. Chen).

https://doi.org/10.1016/j.jallcom.2019.03.191
0925-8388/

oppositely oriented, forming a ferrimagnetic configuration [14,15]. Unlike γ-Fe_2O_3, which is an insulator, Fe_3O_4 is reported to be a semiconductor at room temperature [16].

Enhanced magnetization was reported for Fe_3O_4 capped with alginic acid [17]. This enhancement was attributed to encapsulation-improved Fe_3O_4 surface crystallinity. Intrinsic electronic origins accounting for magnetization enhancement in the Fe_3O_4/graphene heterostructure were also predicted from first-principle calculations [18]. *A*-site irons in Fe_3O_4 were concluded to play a crucial role in determining the magnetism of heterosystems. This conclusion explained the intrinsic electronic effect engendering ferrimagnetic enhancement and prompt our studies on magnetic behavior of carbon-encapsulated magnetite core–shell NPs. Fe_3O_4/carbon core–shell NPs (Fe_3O_4@C NPs) can be synthesized through various approaches, including solvothermal, mechanochemical, and thermal decomposition methods as well as hydrothermal synthesis [12,19–22]. Nevertheless, to the best our knowledge, magnetic enhancement in a carbon-encapsulated magnetite system has not been reported. A carbon shell is usually formed through a high-temperature annealing process, which carbonizes hydrocarbon precursors but also reduces iron oxide [23]. To avoid this reduction, a low-temperature carbon encapsulation procedure was employed.

In this paper, we report that room-temperature ferrimagnetic enhancement can be achieved by controlling the amount of starch precursor used when forming Fe_3O_4@C NPs hydrothermally. The preparation temperature during the hydrothermal process was found to be crucial for the carbonization of the starch precursor and therefore for magnetic enhancement. Transmitting optical magnetic circular dichroism (OMCD) confirmed the existence of interfacial charge transfer in Fe_3O_4@C NPs which engendered the enhancement of ferrimagnetism; that is equivalent to the chemical reduction of the Fe^{3+} in the *A*-site caused by carbon encapsulation. From our experimental observations, the band alignment of a Fe_3O_4@C heterosystem was deduced. The rest of this paper is organized as follows. Section 2 describes the sample preparation and the experimental setups. Section 3 presents the structural [X-ray diffractometry (XRD), Raman spectroscopy, and transmission electron microscopy (TEM)] and magnetic [using a vibrating-sample magnetometer (VSM)] characterization results. In Section 4, to explain the observed ferrimagnetic enhancement, we discuss the channels of charge transfer that possibly occurred in the Fe_3O_4 core based on electronic configuration description. Main optical transitions in Fe_3O_4 based on band descriptions are delivered. The results of OMCD experiments for determining the existence of interfacial charge transfer in the Fe_3O_4@C NPs are presented. Band alignment of the carbon-encapsulated Fe_3O_4 heterosystem suggested by our VSM and OMCD experiments is also proposed. Section 5 gives the conclusions.

2. Experimental procedure

2.1. Sample preparations

Magnetite NPs were synthesized in an aqueous solution through the coprecipitation method. Magnetite NPs were prepared by slowly adding NH_4OH to an aqueous mixture of FeCl3·6H2O and FeSO4·7H2O at a 1:1 M ratio until pH was equal to 10 at room temperature. The black iron oxide product was found to be strongly magnetic. To isolate NPs, the black particles were separated from the liquid by using a bar magnet and were washed with absolute ethanol. This separation and rinsing process was repeated three times. The final product was dried under vacuum at room temperature.

Fe_3O_4@C NPs were prepared through a hydrothermal method, in which pristine 0.5-g Fe_3O_4 NPs were dispersed in deionized water containing soluble starch, as previously described [9]. The resulting suspensions were transferred to the autoclave and maintained at 160 and 200 °C for 12 h. After completion of the reaction, the autoclave was cooled, and the resulting Fe_3O_4@C NPs were collected using a magnet. The final product was washed with deionized water and subsequently dried under vacuum at room temperature. XRD was first conducted to examine the crystalline phases of oxidization and the mean particle size for all prepared samples. Subsequently, the structural stability of the core–shell NPs was evaluated through Raman experiments that utilized samples produced from various amounts of starch precursor as well as at different preparation temperatures during the hydrothermal process. Saturation magnetization measurements were employed to determine the sample with the greatest magnetization and thus the most enhanced ferrimagnetism. This sample was further analyzed using TEM and OMCD. Hereafter, the carbon-encapsulated magnetite samples described are denoted as Fe_3O_4@C; Fe_3O_4@C-160 and Fe_3O_4@C-200 explicitly refer to samples prepared at 160 and 200 °C during the hydrothermal process, respectively.

2.2. Experimental setup

XRD was performed using a BL01C beamline at the National Synchrotron Radiation Research Center in Taiwan. A monochromatic X-ray with a wavelength of 0.6888 Å was used as the probing source. Raman measurements were performed using a microscopic Raman system (RAMaker, Protrustech Co., Ltd., Tainan, Taiwan). An exciting line of 532 nm was supplied by a diode laser (CNI) with a power of 1 mW. The exposure time was 60 s with two accumulations. Calibration was conducted using a silicon standard where the band is generally observed at 520 cm^{-1}. The corresponding spectral resolution was in the range of 1 cm^{-1}. Saturation magnetization and *M*–*H* loop measurements were performed using a VSM (Lake Shore Model 7400, USA) under magnetic fields (*H*) up to 15,000 G. Particle sizes and shapes were studied through TEM on a JEOL JEM-2100F CS STEM. TEM samples were prepared by placing one drop of a dilute particle suspension in anhydrous alcohol on a carbon-coated copper grid and evaporating the solvent at room temperature. For OMCD measurement, a photoelastic modulator in the system (Jasco J-815) produced left-circularly polarized and right-circularly polarized light waves for the measurement. The light source was a 450-mW Xenon lamp; wavelength accuracy was ±0.3 at 250–500 nm and ±0.8 at 500–800 nm. All measurements were performed at room temperature.

3. Structural and magnetic characterization

3.1. XRD phase analysis

Fig. 1 shows the XRD results for the Fe_3O_4@C and pristine Fe_3O_4 samples. The Fe_3O_4@C samples exhibited similar patterns as as-prepared Fe_3O_4, suggesting the crystalline form was nearly unchanged during the hydrothermal process. The diffraction peaks could be indexed to a spinel structure of either magnetite (JCPDS no. 75-0449) or maghemite (JCPDS no. 89-5892). Phase identification of magnetite and maghemite through conventional XRD is not simple, because both have the same cubic structure with a minute distinction in lattice parameters. The (511) peak could be deconvoluted to identify and quantify mixed magnetite/maghemite [24]. Accordingly, most of the crystalline phases in the pristine Fe_3O_4 NPs were magnetite (approximately 86%), and the Fe_3O_4@C samples in the study were nearly pure magnetite. However, a small amount of the hematite phase (α-Fe_2O_3) was detected both in the

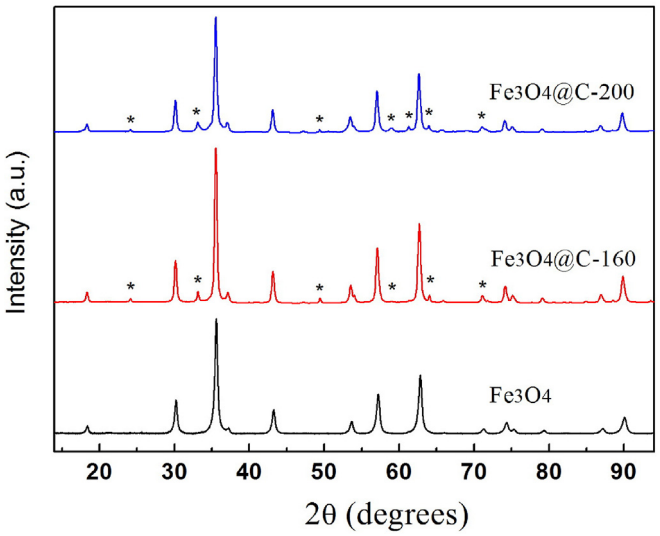

Fig. 1. XRD patterns of Fe_3O_4, Fe_3O_4@C-160, and Fe_3O_4@C-200 samples.*: peaks of hematite.

Fe_3O_4@C-160 and Fe_3O_4@C-200 samples. No additional crystalline phase apart from α-Fe_2O_3 after hydrothermal treatment was concluded. The average crystallite sizes (D_{311}) of the Fe_3O_4, Fe_3O_4@C-160, and Fe_3O_4@C-200 samples were estimated to be 18, 24, and 25 nm, respectively, through Scherrer's formula [25].

3.2. Raman analysis

Fig. 2 shows the Raman spectrum for the phase identifications of the samples prepared from various amounts of the starch precursor. For the magnetite NPs, which were more prone to oxidation by laser heating, the output power of the Raman excitation source was reduced to 1 mW. The spectrum of the as-prepared Fe_3O_4 powder had a main peak at 660–680 nm, consistent with the peaks described in the related literature [26]. All Fe_3O_4@C in this region were in accordance with the characteristic bands of magnetite. In the high wavenumber region (1100–1800 cm^{-1}), the Fe_3O_4@C-200 samples exhibited a typical spectrum of diamond-like carbon [27].

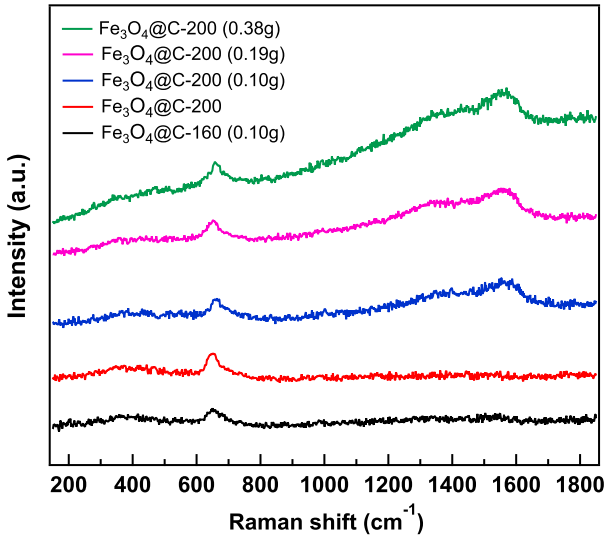

Fig. 2. Raman spectra of pristine and carbon-encapsulated Fe_3O_4 NPs. The amount of starch precursor used (g) is given in parentheses.

This band region could be deconvoluted into a broad band at 1540–1580 cm^{-1} (G band) and another band at 1330–1350 cm^{-1} (D band). The intensity ratio (I_D/I_G) was found to correlate linearly with the sp^2/sp^3 ratio [27]. The I_D/I_G ratios remained nearly the same (approximately 4) for the samples prepared from various amounts of starch. The sp^2/sp^3 ratio was estimated to be approximately 2.5 based on the data reported by Ferrari and Robertson [27,28]. Moreover, I_D and I_G became more prominent when more starch was used as a carbon source when forming the Fe_3O_4@C-200, whereas those in Fe_3O_4@C-160 were severely suppressed, suggesting that the starch was not fully carbonized through hydrothermal treatment at 160 °C. According to our Raman analysis, the hydrothermal carbonization process converted organic starch into a carbon-like product at 200 °C.

3.3. Saturation magnetization and M–H loop measurements

Fig. 3 shows the saturation magnetization (M_s) of pristine Fe_3O_4 NPs (approximately 89 emu/g) and Fe_3O_4@C-200 samples; the mean crystallite sizes estimated from XRD and TEM are also indicated. M_s increased initially until reaching a maximum value of 134 emu/g when approximately 0.19 g of starch precursor before gradually decreasing when additional starch content was used. Both TEM and Scherrer's analyses show a consistent diameter growth of ~1.5 times with carbon encapsulation, but saturate and then slightly decrease with the increasing amount of starch precursor. Possible explanation for the decreasing crystallite size of Fe_3O_4@C-200 was that a large amount of starch facilitates the heterogeneous polymerization on the surface of magnetite, thus hindering the further growth of magnetite NPs.

The M_s of Fe_3O_4@C-200 was usually higher than that of the pristine samples. The significantly decreased M_s of samples that were prepared using as much starch as the carbon precursor can be explained by the relatively low Fe_3O_4 quantity because the difference in the mean crystallite size revealed by XRD was only in the range of 2 nm. These observations suggest that the room-temperature ferrimagnetic enhancement can be achieved through precise control of the amount of starch precursor. The effect of the preparation temperature on M_s was also examined using samples produced from the same amount of starch (0.19 g) precursor added

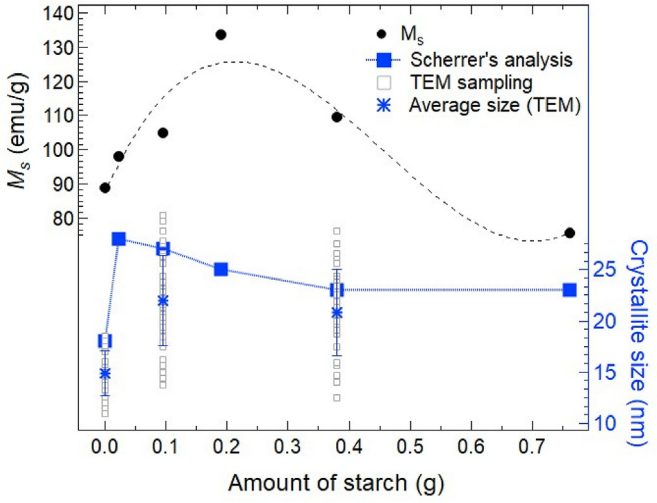

Fig. 3. Saturation magnetization (M_s) and crystallite size of Fe_3O_4@C-200 produced from various amounts of starch precursor. The possible path is displayed by a dotted line. TEM sampling size for pristine Fe_3O_4, Fe_3O_4@C-200 (0.095 g starch) and Fe_3O_4@C-200 (0.38 g starch) are 58, 66, and 70 ea., respectively. Error bars represent the standard deviations of particle size from TEM sampling.

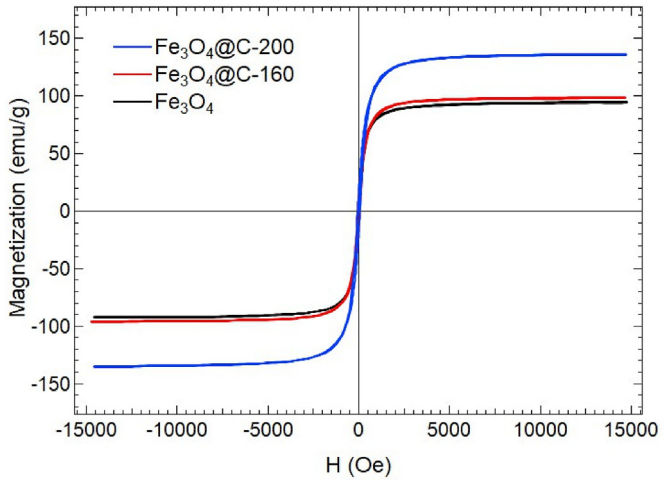

Fig. 4. Magnetization curves of as-prepared Fe_3O_4 NP, Fe_3O_4@C-160, and Fe_3O_4@C-200 (0.19 g starch precursor) samples, as measured through VSM at room temperature.

in the hydrothermal process. Fig. 4 shows the *M*–*H* loops of the as-prepared Fe_3O_4 NPs, Fe_3O_4@C-160, and Fe_3O_4@C-200 samples. All displayed nearly superparamagnetic behavior. The M_s value of Fe_3O_4@C-200 was significantly higher than those of the Fe_3O_4@C-160 and Fe_3O_4 powders. The crystalline phase and the mean crystallite size shown on XRD were almost the same for Fe_3O_4@C-160 and Fe_3O_4@C-200. Therefore, the observed 35% magnetic enhancement of Fe_3O_4@C-200 was primarily related to the formation of the core–shell interface in Fe_3O_4@C.

3.4. TEM measurements

Fig. 5 shows the TEM images of as-prepared Fe_3O_4 and Fe_3O_4@C-200 produced from 0.19 g of the starch precursor. The dark core of the Fe_3O_4 NPs and the grey carbon shell are clearly observable in the TEM image of the Fe_3O_4@C-200 sample. Although the Fe_3O_4@C-200 sample was enlarged after the hydrothermal process, the *Ms* have shown excessively higher than the bulk Fe_3O_4 (92 emu/g) at room temperature [13], suggesting the intrinsic electronic origins rather than NP size effect were accounted for the observed ferrimagnetic enhancement. To the best of our knowledge, the observation of room-temperature magnetic enhancement in amorphous carbon-encapsulated magnetite NPs has not been reported elsewhere. The typical carbon shell thickness was estimated to be 2 nm, and that may suggest the appropriate diameter-to-thickness ratio of Fe_3O_4@C NPs is a prerequisite for observation of this enhancement.

4. Origins of magnetic enhancement

4.1. Electronic configuration description

In this section, we discuss the charge transfer that possibly occurs to explain the observed ferrimagnetic enhancement based on the electronic configuration of Fe_3O_4. The cubic phase of Fe_3O_4 comprises a mixture of Fe^{3+} and Fe^{2+} ions in the *B*-site, whereas only Fe^{3+} ions exist in the *A*-site. The spins of Fe ions in each site are in opposite directions, forming a ferrimagnetic configuration. Following Hund's rule, the high-spin configurations for each subcell are as follows: the Fe^{3+} (d^5) in the *A*-site can be represented by ($e^{2\downarrow}\ t_2^{3\downarrow}$); the Fe^{2+} (d^6) and Fe^{3+} in the *B*-site can be represented by ($t_{2g}^{3\uparrow}\ e_g^{2\uparrow}\ t_{2g}^{\downarrow}$) and ($t_{2g}^{3\uparrow}\ e_g^{2\uparrow}$), respectively. Here, the notations $^{\uparrow}$ and $^{\downarrow}$ denote spin direction parallel (majority) and antiparallel (minority) to total magnetization ($\uparrow$). We suggest that two channels possibly account for the experimentally observed magnetic enhancement. First, a $^{\uparrow}$ electron may be transferred to the empty *e* state of the *A*-site Fe^{3+} [*A*(*e*)], which is equivalent to the chemical reduction of Fe^{3+} in the *A*-site; second, a $^{\downarrow}$ electron may be removed from the t_{2g} state of the *B*-site Fe^{2+} [$B(t_{2g}^{\downarrow})$], which is equivalent to the oxidization of Fe^{2+} in the *B*-site. Here, we use the formulae $e^{2\downarrow}\ t_2^{3\downarrow}\ e \rightarrow e^{2\downarrow}\ t_2^{3\downarrow}\ e^{\uparrow}$ and $t_{2g}^{3\uparrow}\ e_g^{2\uparrow}\ t_{2g}^{\downarrow} \rightarrow t_{2g}^{3\uparrow}\ e_g^{2\uparrow}\ t_{2g}$ (denotes the empty state to/from which a polarized electron is transferred) to represent the two possibilities accounting for the observed saturation moment enhancement of Fe_3O_4@C-200. Each represents electron addition to the *e* state of the *A*-site and electron removal from the t_{2g} state of the *B*-site, respectively. Both cases explain the increase in total magnetic moment but with opposite flow directions and sign of spin that may occur in the Fe_3O_4@C heterosystem.

Amorphous carbon (*a*-C) contains both a three-fold coordinated sp^2 configuration, as in graphite, and four-fold sp^3 sites, as in diamond. For sp^3 sites, each of the four valence electrons lies in a sp^3 hybrid, which then forms a σ bond with a neighbor. At a sp^2 site, only three of these electrons are used in the σ bonds; the fourth enters a π orbital that lies normal to the σ-bond plane. The π states are only weakly bonded and therefore are the most likely electron donors at the heterointerface, which infers that the transfer of the π electron to the *A*-site of Fe_3O_4 engenders the ferrimagnetic magnetic enhancement.

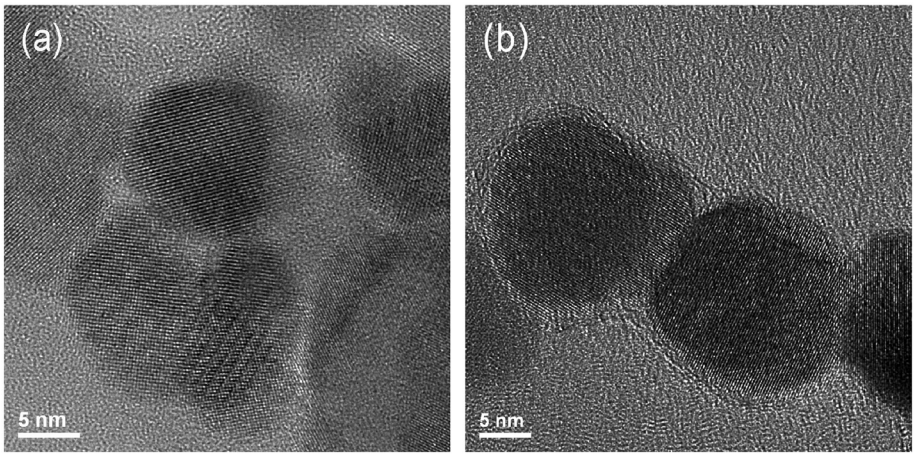

Fig. 5. High-resolution TEM bright-field images of (a) as-prepared Fe_3O_4 NPs and (b) Fe_3O_4@C-200 NPs (0.19 g starch precursor).

4.2. Electronic structure and spin-dependent optical transitions in magnetite

Density functional theory (DFT) employing Hubbard-*U* correction (DFT + *U*) [29] has proven to be essential for describing Fe_3O_4 in terms of optical and magnetic properties [30–35]. On-site Coulomb interactions (*U*) rectify the overestimated *p-d* hybridization and provide accurate energy positions for both occupied and unoccupied states. Our recent studies [30] have concluded that the transmitting OMCD spectra can describe the valence electronic structures after consideration of electron correlation effects, and hence the dominant spin-dependent optical transition in magnetite. Fig. 6(a) shows the spin-polarized projected density of states of Fe_3O_4. The valence structure comprises mainly crystal field splitting of Fe(*3d*) into t_{2g} and e_g group hybridized with O(*2p*) bands. The notable half-metallicity is indicated by the *B*-site t_{2g} spin-minority band, denoted by $B(t_{2g})\downarrow$, across by the Fermi level (E_F). A valence gap of spin-majority (~2.2 eV) is formed by the unoccupied electronic states of *A*-site, denoted by $A(e;t_2)\uparrow$, and the occupied $B(e_g)\downarrow$; a relatively smaller valence gap of spin-minority (~2.0 eV) is formed by $B(t_{2g})\downarrow$ and $O(2p)\downarrow$. The most relevant to optical transition in UV–VIS region is the band interval between binding energy 2 and -6 eV, of which the spin-majority and -minority are dominated by polarized Fe(*3d*) and O(*2p*) bands, respectively. The occupied electronic states of *A*-site [$A(e;t_2)\downarrow$] are located deeper beyond this region, and $A(e;t_2)\uparrow$ immediately above the E_F is fully empty.

Fig. 6(b) shows the schematic site-projected density of states of Fe_3O_4, in which the main optical transitions are depicted by arrows. Main transitions are categorized into three types, namely of intra-site, intersite, and ligand-to-metal optical transition. They are also known as intervalence charge transfer (IVCT), intersublattice charge transfer (ISCT), and ligand-to-metal charge transfer (LMCT), respectively. The IVCT relaxing from Laporte selection is mainly minority-spin transfer of $B(t_{2g})\downarrow \rightarrow B(e_g)\downarrow$; the ISCT, mediated by *2p* oxygen, is the majority-spin transfer of $B(e_g)\uparrow \rightarrow A(e;t_2)\uparrow$. The LMCT is the minority-spin transfer of $O(2p)\downarrow \rightarrow B(t_{2g})\downarrow$.

4.3. OMCD measurement

OMCD in Faraday geometry manifesting the absorptive difference of incident photons with spins parallel ($\boldsymbol{\sigma}_+$) and antiparallel ($\boldsymbol{\sigma}_-$) to the applied magnetic field was recorded simultaneously as a function of wavelength. With the resolution of both energy and dominant absorptive spin-channel, the OMCD signal ($\boldsymbol{\sigma}_+ - \boldsymbol{\sigma}_-$) can resolve the dominant channels of spin-dependent optical transition in a spin-split valence system. This technique enables a simple laboratory probe for the interfacial charge transfer in the nanocomposite through observations of the relative shift of spectrum between the pristine Fe_3O_4 NPs and the Fe_3O_4@C heterosystem. Fig. 7 shows the OMCD spectra of pristine Fe_3O_4 NPs and Fe_3O_4@C-200 at the zero field and the saturation field of ±0.8 T. The OMCD profile of the pristine Fe_3O_4 NPs is consistent with that described in the literature [37–39]. It mainly comprises regions according to the sign of the OMCD signal. The interval of negative OMCD from pristine Fe_3O_4 NPs 1.50–2.30 eV, as depicted in Fig. 7 (c), is attributed to the IVCT of $B(t_{2g})\downarrow \rightarrow B(e_g)\downarrow$ [dotted line in Fig. 6 (b)] i.e., the crystal-field transition [40] of the *B*-site. The broad band with positive OMCD (2.30–4.00 eV) mainly reflects the competition between the ISCT of $B(e_g)\uparrow \rightarrow A(e;t_2)\uparrow$ [dashed line in Fig. 7 (b)] and the LMCT of $O(2p)\downarrow \rightarrow B(t_{2g})\downarrow$ [solid line in Fig. 7 (b)], which are characterized by the paramagnetic response of the main raising edge (2.30–2.86 eV) and the diamagnetic response of the falling edge (2.86–4.00 eV) in the broad band, respectively. Note that the onset of ISCT define the optical gap of spin majority, which was enlarged for Fe_3O_4@C-200 as suggested from the OMCD blue shift (0.25-eV) of the main raising edge. This blue shift can also be considered from the work function difference of the core-shell material. The work function ($\varnothing$) of *a*-C determined by Keivin probe can vary in the range 4–5 eV [41]; that of bulk Fe_3O_4 was reported to be 5.78 eV, truncated to 5.32 eV at the surface [42,43]. Hence, the Fe_3O_4@C heterosystem can be represented by a metal to magnetic-semiconducting contact of the case $\varnothing_m < \varnothing_{ms}$, which also indicates the charge flow direction is from the metal (*a*-C) to the semiconducting (Fe_3O_4) side. The shift value of 0.25-eV is close to the work function difference ($\varnothing_m - \varnothing_{ms}$), suggesting the channel of

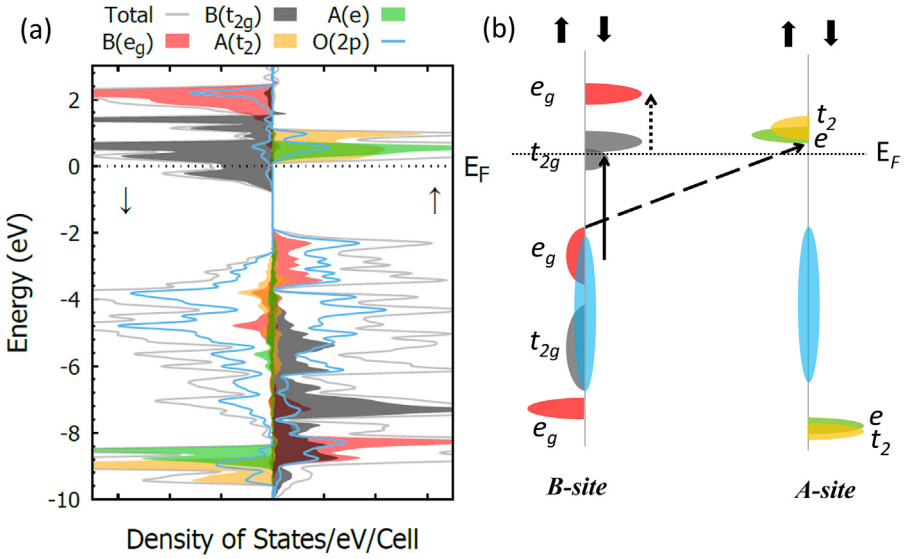

Fig. 6. (a) Spin-polarized projected density of states (PDOS) of Fe_3O_4 ($Fd\bar{3}m$) calculated through DFT + *U* as implemented in Vienna Ab initio Simulation Package (VASP) [36]. (Left panel) Minority-spin DOS; (Right) majority-spin DOS. The simulation is $Fe_A(8)Fe_B(16)O(32)$ with 56 total atoms in a cell of ferrimagnetic configuration. The Fermi level (E_F) is indicated by the dotted horizontal line. For calculation details refer to Ref. [30]. (b) Schematic of valence band electronic structure and associated optical transitions in Fe_3O_4. Dotted, dashed, and solid lines represent the inter-valence charge transfer (IVCT), inter-sublattice charge transfer (ISCT), and ligand-to-metal charge transfer (LMCT) which corresponding to minority-spin transfer of $B(t_{2g})\downarrow \rightarrow B(e_g)\downarrow$, majority-spin transfer of $B(e_g)\uparrow \rightarrow A(e;t_2)\uparrow$, and minority-spin transfer of $O(2p)\downarrow \rightarrow B(t_{2g})\downarrow$, respectively.

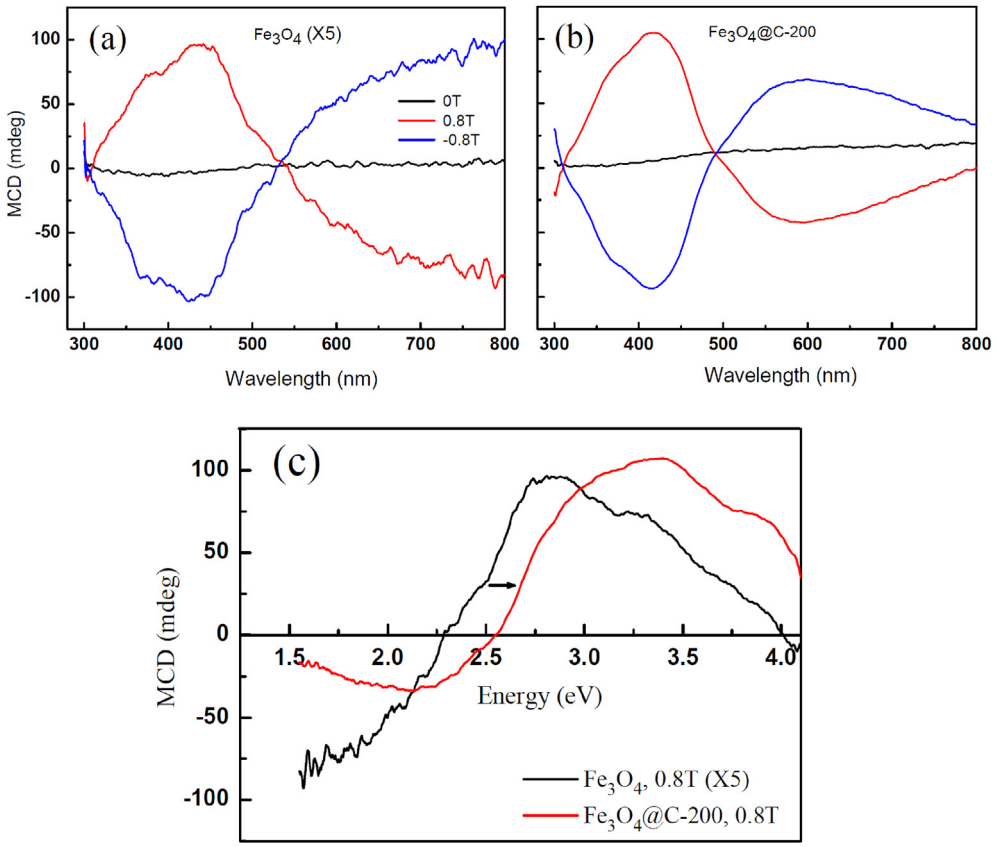

Fig. 7. OMCD spectra of (a) pristine Fe_3O_4 NPs and (b) Fe_3O_4@C-200 samples. (c) Overlapping of these two curves (eV) under the applied voltage of 0.8 T. Blue shift of the main raising edge representing ISCT of $B(e_g)\uparrow \rightarrow A(e;t_2)\uparrow$ [dashed line in Fig. 6(c)] is indicated by the arrow. (For interpretation of the references to color in this figure legend, the reader is referred to the Web version of this article.)

electron addition in the *A*-site Fe^{3+} ($e^{2\downarrow}\ t_2^{3\downarrow}\ e \rightarrow e^{2\downarrow}\ t_2^{3\downarrow}\ e^{\uparrow}$) of Fe_3O_4@C-200 due to carbon encapsulation. Therefore, the OMCD blue shift have implied the charge transfer into the polarized *e* band of the *A*-site.

4.4. Band alignment

The observations of the ferrimagnetic enhancement and the OMCD blue shift of Fe_3O_4@C-200 sample have indicated the existence of spin-polarized interfacial charge transfer in a core–shell heterosystem. We propose the band alignment of the Fe_3O_4@C heterosystem, as shown in Fig. 8. Two isolated systems of $\varnothing_m < \varnothing_{ms}$ were referred to a common vacuum level. The band descriptions of *a*-C generally suggest the π states lie on the E_F [43]. We focused on the bands of majority spin, which essentially account for the ferrimagnetic enhancement. The conduction band maximum (CBM) and valence band minimum (VBM) of Fe_3O_4 are represented by $A(e;t_2)\uparrow$ and $B(e_g)\uparrow$, respectively. The optical gap of the majority spin joining the CBM and VBM is approximately 2.0 eV. When forming the contact, the π electrons in the vicinity of the E_F flow into the polarized $A(e;t_2)\uparrow$ band until the induced dipole field brings the E_F on the two sides together, and that leads to the magnetic moment enhancement in Fe_3O_4@C-200 as well as the increasing optical gap of majority spin. The later engendering the OMCD blue shift (approximately 0.25 eV) as well as the ferrimagnetic enhancement was demonstrated by a valence band offset (Δ_{VBO}) of the Fe_3O_4@C heterosystem.

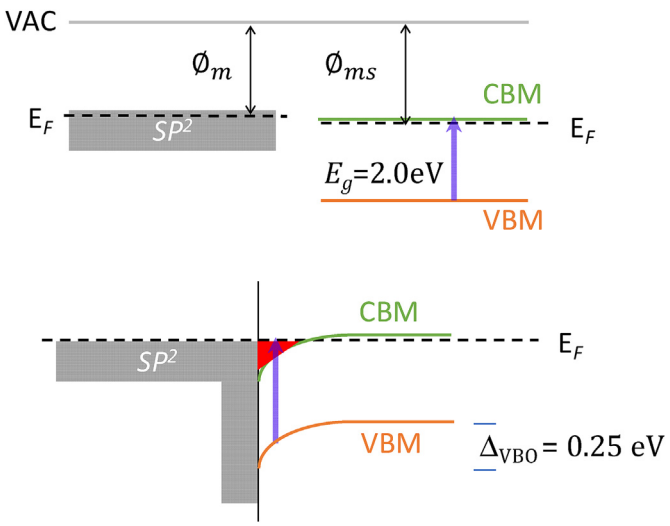

Fig. 8. (Top) Schematic diagram of valence electron states of isolated amorphous carbon (*a*-C) and Fe_3O_4. Vacuum level and Fermi energy are indicated by VAC and E_F (thin dashed line), respectively. CBM and VBM are represented by the unoccupied state of the *A*-site [$A(e;t_2)\uparrow$] and the occupied state of *B*-site [$B(e_g)\uparrow$]; $\varnothing_m$ and $\varnothing_{ms}$, as indicated by the arrow lines, are work functions of *a*-C (metal) and Fe_3O_4 (magnetic-semiconductor). The optical gap of majority spin (E_g) is indicated by the thick arrow joining VBM and CBM. (Bottom) Band alignment in representing Fe_3O_4@C as a metal-to-magnetic semiconducting contact. The heterointerface is indicated by the thin vertical solid line. The valence band offset ($\Delta_{VBO} = 0.25$ eV) of the heterosystem obtained through OMCD measurement is also indicated.

5. Conclusions

The magnetization properties of carbon-encapsulated Fe_3O_4 NPs synthesized through chemical coprecipitation were examined in this study. Fe_3O_4/C particles were formed through the hydrothermal method, with the Fe_3O_4 NPs as a magnetic core and soluble starch as a carbon source. The M_s of Fe_3O_4@C samples was generally higher than that of pristine Fe_3O_4 after hydrothermal treatment at 200 °C. The magnetite–carbon interface charge transfer played a major role in the increase in ferrimagnetic magnetization. We proposed the observed 35% magnetic enhancement was primarily caused by charge transfer from carbon to the *A*-site of the Fe_3O_4 because of the observed blue shift in the OMCD spectrum. The enhancement of room-temperature ferrimagnetism in Fe_3O_4@C was attributed to electron addition of the *A*-site Fe^{3+}, which was equivalent to the chemical reduction of *A*-site irons of Fe_3O_4, due to carbon encapsulation. We conclude that the Fe_3O_4@C forms a heterojunction so that the *a*-C passivates the magnetic semiconducting Fe_3O_4 microcrystalline particles, to which the sp^2 electron is transferred. The proposed Fe_3O_4@C NPs with higher M_s and stability than those of pure Fe_3O_4 can benefit biomedical applications.

Acknowledgements

The authors would like to thank the Ministry of Science and Technology, R.O.C. for financially supporting this research under MOST 106-2112-M-153-003.

References

[1] J. Jiao, S. Seraphin, Carbon encapsulated nanoparticles of Ni, Co, Cu, and Ti, J. Appl. Phys. 83 (8) (1998) 2442–2448.
[2] C.F. Wang, J.N. Wang, Z.M. Sheng, Solid-phase synthesis of carbon-encapsulated magnetic nanoparticles, J. Phys. Chem. C 111 (17) (2007) 6303–6307.
[3] X. Fang, X. Cheng, Y. Zhang, L.G. Zhang, M. Keidar, Single-step synthesis of carbon encapsulated magnetic nanoparticles in arc plasma and potential biomedical applications, J. Colloid Interface Sci. 509 (2018) 414–421.
[4] J. Kim, J.E. Lee, S.H. Lee, J.H. Yu, J.H. Lee, T.G. Park, et al., Designed fabrication of a multifunctional polymer nanomedical platform for simultaneous cancer-targeted imaging and magnetically guided drug delivery, Adv. Mater. 20 (3) (2008) 478–483.
[5] J. Kim, S. Park, J.E. Lee, S.M. Jin, J.H. Lee, I.S. Lee, et al., Designed fabrication of multifunctional magnetic gold nanoshells and their application to magnetic resonance imaging and photothermal therapy, Angew. Chem. Int. Ed. 45 (46) (2006) 7754–7758.
[6] J. Yu, D. Huang, M.Z. Yousaf, Y. Hou, S. Gao, Magnetic nanoparticle-based cancer therapy, Chin. Phys. B 22 (2) (2013) 027506–027513.
[7] K. Cheng, S. Peng, C. Xu, S. Sun, Porous hollow Fe_3O_4 nanoparticles for targeted delivery and controlled release of cisplatin, J. Am. Chem. Soc. 131 (30) (2009) 10637–10644.
[8] W. Wu, Z. Wu, T. Yu, C. Jiang, W.-S. Kim, Recent progress on magnetic iron oxide nanoparticles: synthesis, surface functional strategies and biomedical applications, Sci. Technol. Adv. Mater. 16 (2) (2015) 023501–023543.
[9] S.-N. Sun, C. Wei, Z.-Z. Zhu, Y.-L. Hou, S.S. Venkatramana, Z.-C. Xu, Magnetic iron oxide nanoparticles:Synthesis and surface coating techniques for biomedical applications, Chin. Phys. B 23 (3) (2014), 037503-19.
[10] T. Biswal, B. Barik, P.K. Sahoo, Synthesis and characterization of magnetite-pectin-alginate hybrid bionanocomposite, J. Mater. Sci. Technol. 4 (2) (2016) 1–8.
[11] R. Frison, G. Cernuto, A. Cervellino, O. Zaharko, G.M. Colonna, A. Guagliardi, et al., Magnetite–maghemite nanoparticles in the 5–15 nm range: correlating the core–shell composition and the surface structure to the magnetic properties. A total scattering study, Chem. Mater. 25 (23) (2013) 4820–4827.
[12] E. Rafiee, M. Khodayari, Starch as a green source for Fe_3O_4@carbon core–shell nanoparticles synthesis: a support for 12-tungstophosphoric acid, synthesis, characterization, and application as an efficient catalyst, Res. Chem. Intermed. 42 (4) (2016) 3523–3536.
[13] H. Shokrollahi, A review of the magnetic properties, synthesis methods and applications of maghemite, J. Magn. Magn. Mater. 426 (2017) 74–81.
[14] M.K. Niranjan, J.P. Velev, C.G. Duan, S.S. Jaswal, E.Y. Tsymbal, Magnetoelectric effect at the Fe_3O_4/$BaTiO_3$(001) interface: a first-principles study, Phys. Rev. B 78 (10) (2008) 104405–104408.
[15] T. Kida, S. Honda, H. Itoh, J. Inoue, H. Yanagihara, E. Kita, et al., Electronic and magnetic structure at the Fe/Fe_3O_4 interface, Phys. Rev. B 84 (10) (2011) 104407.
[16] H.E. Ghandoor, H.M. Zidan, M.M.H. Khalil, M.I.M. Ismail, Synthesis and some physical properties of magnetite (Fe3O4) nanoparticles, Int. J. Electrochem. Sci. 7 (2012) 5734–5745.
[17] B. Andrzejewski, W. Bednarski, M. Kazmierczak, K. Pogorzelec-Glaser, B. Hilczer, S. Jurga, et al., Magnetization enhancement in magnetite nanoparticles capped with alginic acid, Composites Part B 64 (2014) 147–154.
[18] W. Mi, H. Yang, Y. Cheng, G. Chen, H. Bai, Magnetic and electronic properties of Fe_3O_4/graphene heterostructures: first principles perspective, J. Appl. Phys. 113 (8) (2013), 083711-7.
[19] D. Shi, H. Yang, S. Ji, S. Jiang, X. Liu, D. Zhang, Preparation and characterization of core-shell structure Fe_3O_4@C magnetic nanoparticles, Procedia Eng. 102 (2015) 1555–1562.
[20] A.K. Gupta, M. Gupta, Synthesis and surface engineering of iron oxide nanoparticles for biomedical applications, Biomaterials 26 (18) (2005) 3995–4021.
[21] M. Arana, S.E. Jacobo, H. Troiani, P.G. Bercoff, Synthesis and characterization of carbon-coated magnetite for functionalized ferrofluids, IEEE Trans. Magn. 49 (8) (2013) 4547–4550.
[22] J.-S. Qiu, Y.-F. Sun, Y. Zhou, T.-J. Sun, Q.-X. Li, Preparation and magnetic properties of carbon encapsulated iron nanocapsules from starch, N. Carbon Mater. 21 (3) (2006) 202–205.
[23] R.G. Mendes, B. Koch, A. Bachmatiuk, A.A. El-Gendy, Y. Krupskaya, A. Springer, et al., Synthesis and toxicity characterization of carbon coated iron oxie nanoparticles with highly defined size distributions, Biochim. Biophys. Acta 1840 (1) (2014) 160–169.
[24] W. Kim, C.-Y. Suh, S.-W. Cho, K.-M. Roh, H. Kwon, K. Song, et al., A new method for the identification and quantification of magnetite–maghemite mixture using conventional x-ray diffraction technique, Talanta 94 (2012) 348–352.
[25] A.L. Patterson, The Scherrer formula for x-ray particle size determination, Phys. Rev. 56 (10) (1939) 978–982.
[26] O.N. Shebanova, P. Lazor, Raman study of magnetite (Fe_3O_4): laser-induced thermal effects and oxidation, J. Raman Spectrosc. 34 (11) (2003) 845–852.
[27] F.C. Tai, S.C. Lee, C.H. Wei, S.L. Tyan, Correlation between I_D/I_G ratio from visible Raman spectra and sp^2/sp^3 ratio from XPS spectra of annealed hydrogenated DLC film, Mater. Trans., JIM 47 (7) (2006) 1847–1852.
[28] A.C. Ferrari, J. Robertson, Interpretation of Raman spectra of disordered and amorphous carbon, Phys. Rev. B 61 (20) (2000) 14095–14107.
[29] G. Kresse, J. Hafner, *Ab initio* molecular dynamics for liquid metals, Phys. Rev. B 47 (1) (1993) 558–561.
[30] J. Chen, H.-S. Hsu, Y.-H. Huang, D.-J. Huang, Spin-dependent optical charge transfer in magnetite from transmitting optical magnetic circular dichroism, Phys. Rev. B 98 (8) (2018), 085141-11.
[31] V.I. Anisimov, J. Zaanen, O.K. Andersen, Band theory and mott insulators: hubbard *U* instead of stoner *I*, Phys. Rev. B 44 (3) (1991) 943–954.
[32] D.J. Huang, C.F. Chang, H.-T. Jeng, G.Y. Guo, H.-J. Lin, W.B. Wu, H.C. Ku, A. Fujimori, Spin and orbital magnetic moments of Fe_3O_4, Phys. Rev. Lett. 93 (7) (2004), 077204-4.
[33] I. Leonov, A.N. Yaresko, V.N. Antonov, V.I. Anisimov, Charge and orbital order in Fe_3O_4, Phys. Rev. B 74 (14) (2006), 165117-4.
[34] G. Rollmann, A. Rohrbach, P. Entel, J. Hafner, First-principles calculation of the structure and magnetic phases of hematite, Phys. Rev. B 69 (16) (2004) 165107–165112.
[35] V.N. Antonov, B.N. Harmon, V.P. Antropov, A. Ya. Perlov, A.N. Yaresko, Electronic structure and magneto-optical Kerr effect of Fe_3O_4 and Mg^{2+}- or Al^{3+}-substituted Fe_3O_4, Phys. Rev. B 64 (13) (2001) 134410–134412.
[36] E. Fantechi, G. Campo, D. Carta, A. Corrias, C. de J. Fernandez, D. Gatteschi, et al., Exploring the effect of Co doping in fine maghemite nanoparticles, J. Phys. Chem. C 116 (14) (2012) 8261–8270.
[37] G.A. Gehring, M.S. Alshammari, D.S. Score, J.R. Neal, A. Mokhtari, A.M. Fox, Magneto-optic studies of magnetic oxides, J. Magn. Magn. Mater. 324 (21) (2012) 3422–3426.
[38] M.S. Alshammari, M.S. Alqahtani, H.B. Albargi, S.A. Alfihed, Y.A. Alshetwi, A.A. Alghihab, et al., Magnetic properties of In_2O_3 containing Fe_3O_4 nanoparticles, Phys. Rev. B 90 (14) (2014), 144433-11.
[39] W.F.J. Fontijn, P.J. van der Zaag, L.F. Feiner, R. Metselaar, M.A.C. Devillers, A consistent interpretation of the magneto-optical spectra of spinel type ferrites, J. Appl. Phys. 85 (8) (1999) 5100–5105.
[40] A. Ilie, A. Hart, A.J. Flewitt, J. Robertson, W.I. Milne, Effect of work function and surface microstructure on field emission of tetrahedral amorphous carbon, J. Appl. Phys. 88 (10) (2000) 6002.
[41] T. Kendelewicz, S. Kaya, J.T. Newberg, H. Bluhm, N. Mulakaluri, W. Moritz, et al., X-ray photoemission and density functional theory study of the interaction of water vapor with the Fe_3O_4(001) surface at near-ambient conditions, J. Phys. Chem. C 117 (6) (2013) 2719–2733.
[42] M. Fonin, R. Pentcheva, Yu. S. Dedkov, M. Sperlich, D.V. Vyalikh, M. Scheffler, et al., Surface electronic structure of the Fe_3O_4(100): evidence of a half-metal to metal transition, Phys. Rev. B 72 (10) (2005) 104436–104438.
[43] J. Robertson, E.P. O'Reilly, Electronic and atomic structure of amorphous carbon, Phys. Rev. B 35 (6) (1987) 2946–2957.